ELSEVIER

Materials Chemistry and Physics 57 (1998) 1–16

MATERIALS CHEMISTRY AND PHYSICS

Invited Review

Microcavity engineering by plasma immersion ion implantation

Paul K. Chu[a,*], Nathan W. Cheung[b]

[a] Department of Physics and Materials Science, City University of Hong Kong, Kowloon, Hong Kong

[b] Department of Electrical Engineering and Computer Sciences, University of California, Berkeley, CA 94720, USA

Received 14 July 1998; accepted 5 August 1998

Abstract

Microcavities formed in silicon wafers by hydrogen or helium plasma immersion ion implantation possess very interesting properties. The physical mechanisms of the initiation and coalescence of the microcavities are described using results generated by combination of microscopic, spectroscopic, and other chemical characterization techniques. We will also review three areas that are of interest to the semiconductor industry: light emission, impurity gettering, and ion-cut. The latest results with respect to the fabrication of silicon-on-insulator by the ion-cut technique will also be discussed. © 1998 Elsevier Science S.A. All rights reserved.

Keywords: Plasma; Ion implantation; Silicon

1. Introduction

Plasma immersion ion implantation (PIII) [1] is a burgeoning surface treatment and material synthesis technology for semiconductors [2–5] as the process employs relatively simple and inexpensive instrumentation. As shown in Fig. 1, the sample is placed in a vacuum chamber in which a plasma is sustained by either a radio-frequency (RF) or electron cyclotron resonance (ECR) source. By biasing the sample negatively, ions are implanted into the sample conformally. Because of the absence of beam filtering and collimating optics, the implantation dose rate achieved by PIII can be as high as 10^{16} ions cm^{-2} s^{-1}, which is at least an order of magnitude higher than that of a conventional implanter. In addition, since the entire wafer is implanted simultaneously, the implantation time is independent of the wafer size. This feature has important economical advantage considering that the semiconductor industry is constantly moving towards larger wafers. Furthermore, the PIII reactor setup is simple, easy to maintain, and fully compatible with cluster-tools. The drawback is that all the ions in the plasma, including the unintentional species or contaminants, can be co-implanted if the process is not designed properly. There are many applications of PIII in the semiconductor industry, including shallow junction formation [6–23], passivation of flat-panel display materials [24], conformal deposition [25–33], improvement of low dielectric constant materials [34], and formation of silicon-on-insulator [35–43]. In this paper, we will focus our attention on the characteristics and applications of the microcavities formed by either hydrogen or helium plasma immersion ion implantation. It should, however, be mentioned that conventional beam-line ion implantation can also be employed to fabricate microcavities but the large area processing capability and efficiency of the PIII process makes it the technique of choice for 200 mm and larger silicon wafers.

2. Formation of microcavities by hydrogen plasma immersion ion implantation

When a sufficient dose of hydrogen is implanted into a single crystal silicon wafer, the hydrogen atoms combine with silicon atoms forming Si–H complex in a post-annealing process. The Si–H bond formation has been detected using infrared spectroscopy measurement [44,45]. During thermal annealing, the trapped hydrogen atoms diffuse and segregate near the peak implantation region to form microcavites filled with H_2 molecules. Under further annealing, more hydrogen diffuses into the microcavites, and the high pressure inside the microcavities becomes the driving force for their expansion and growth. As they grow, more hydrogen atoms diffuse in and keep the internal pressure high enough for further expansion. Meanwhile, the microcavities coalesce forming even larger cavities. Fig. 2 displays a

*Corresponding author. Tel.: +852-2788-7724; Fax: +852-2788-7830; E-mail: paul.chu@cityu.edu.hk

0254-0584/98/$ – see front matter © 1998 Elsevier Science S.A. All rights reserved.
PII: S0254-0584(98)00211-9

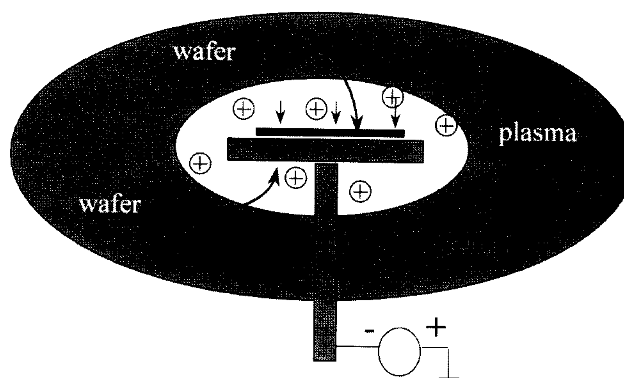

Fig. 1. Schematic of the plasma immersion ion implantation process.

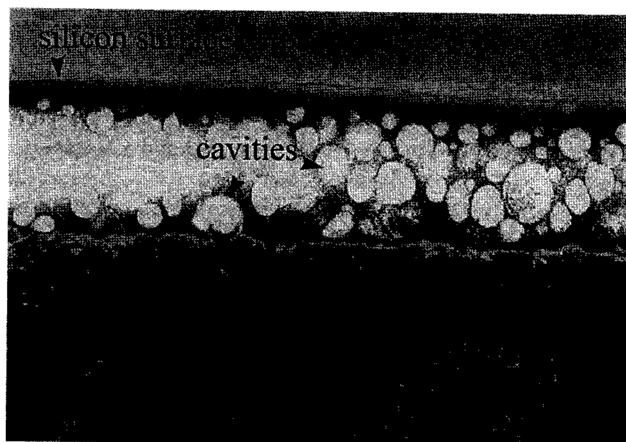

Fig. 2. XTEM micrograph showing the band of buried microcavities.

cross-sectional transmission electron microscopy (XTEM) picture showing a band of buried bubbles or microcavities.

The evolution of the microcavities formed by PIII with temperature has been investigated. A series of surface morphology images acquired by scanning electron microscopy (SEM) is shown in Fig. 3 [41]. In these samples, the hydrogen dose is $4 \times 10^{16}\,cm^{-2}$ and the rapid thermal annealing (RTA) time is 5 min. Microcavities less than 0.5 μm begin to form at 325°C, but they are hardly visible in the picture due to low contrast. When the RTA temperature is raised to 350°C and above, the microcavities become more visible. They grow bigger when the annealing temperature is higher. At 400°C, some microcavities start to break through the silicon surface. This is the early stage of silicon layer breakage utilized in the ion-cut process to be discussed later in this paper. At higher annealing temperatures, more pieces of silicon cleave. When the annealing temperature reaches 500°C and above, the total density of the cleavage area does not increase further even under higher annealing temperature. The normal size of the exfoliated silicon pieces is 2–3 μm and secondary electron microscopy (SEM) confirms the same morphology.

The effects of the hydrogen dose on the exfoliation process has been investigated using similar annealing conditions (5 min RTA) and different hydrogen doses. For a sample with a hydrogen dose of $8 \times 10^{16}\,cm^{-2}$ by PIII, microcavities start to form at 300°C, which is 25°C lower than the sample with a hydrogen dose of $4 \times 10^{16}\,cm^{-2}$. The density of the cleavage area is also higher. It saturates at 450°C, which is also a lower temperature than the sample with a hydrogen dose of $4 \times 10^{16}\,cm^{-2}$ (500°C). For the sample with a hydrogen dose of $4 \times 10^{16}\,cm^{-2}$, a 20 s RTA

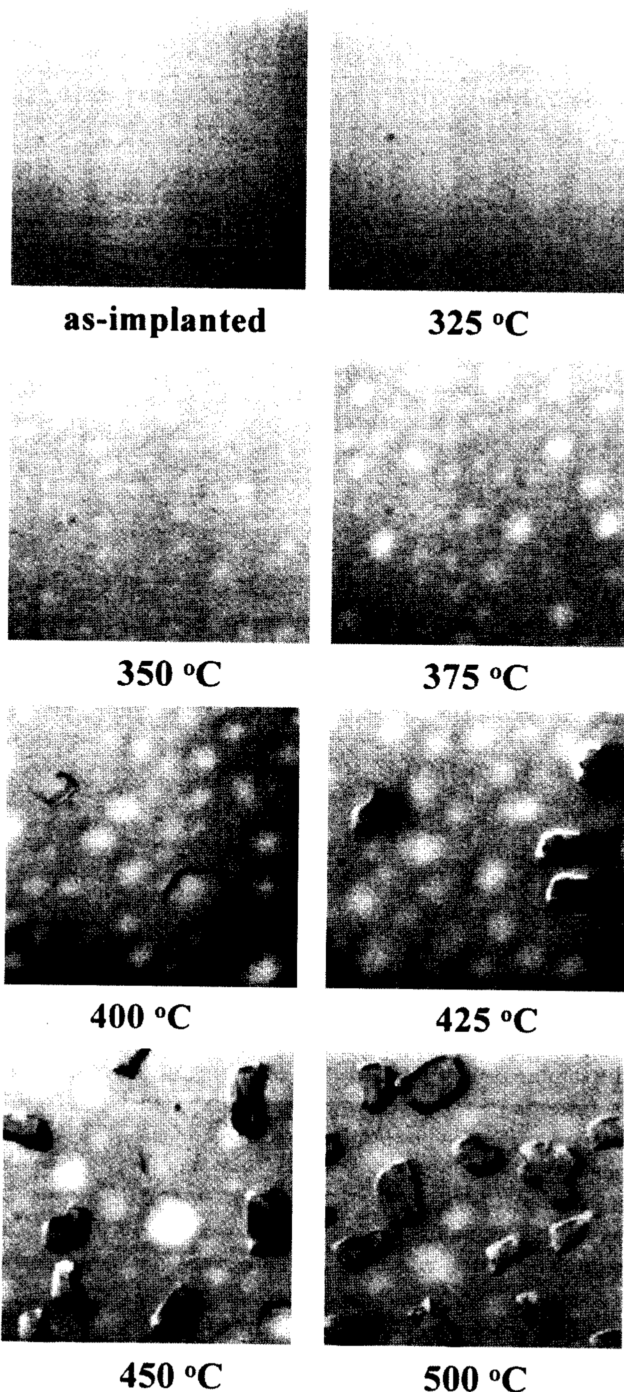

Fig. 3. Optical microscopic surface images of hydrogen implanted sample before and after RTA. All the RTA time duration was 5 min. These samples were implanted at 40 kV at a dose of $4 \times 10^{16}\,cm^{-2}$.

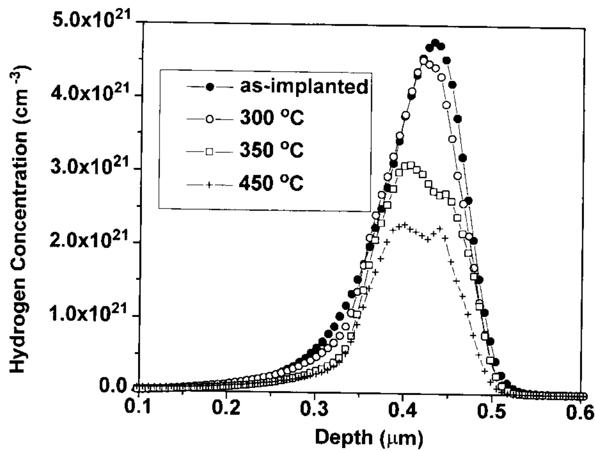

Fig. 4. SIMS hydrogen depth profiles before and after RTA.

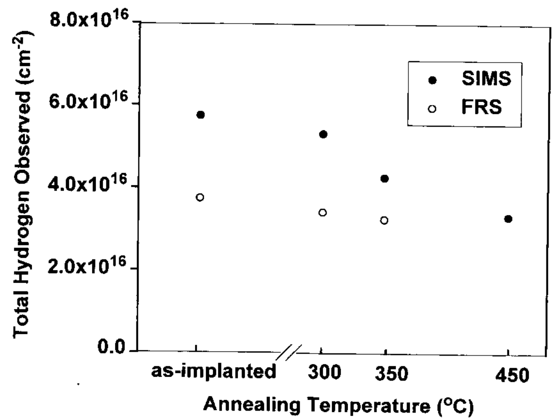

Fig. 5. Total hydrogen dose from both SIMS and HFS measurements before and after RTA. All RTA duration is 5 min. A nominal hydrogen dose of 4×10^{16} cm^{-2} is implanted at 40 kV with H^+ ions.

at 400°C is equivalent to 5 min at 325°C (sub-0.5 μm microcavities becoming visible). Similarly, 1 min at 400°C is equivalent to 5 min at 375°C and 10 min at 400°C is equivalent to 5 min at 425°C. The results suggest that a thermal budget or an activation energy, rather than a critical annealing temperature, is more important for the microcavity nucleation and growth. It can be explained as a temperature–time annealing phenomenon using an activation energy concept [46,47]. However, the activation energies derived form these two reports are slightly different. Tong et al. [46] reports an activation energy of 1.6 eV between 200°C and 500°C. Poumeyrol [47] shows that the activation energy is 2.3 eV between 400°C and 450°C and 0.4 eV between 600°C and 900°C.

A series of hydrogen depth profiles acquired by secondary ion mass spectrometry (SIMS) is plotted in Fig. 4. As shown by the as-implanted profile, the hydrogen peak is located at about 0.43 μm underneath the surface that is in good agreement with the TRIM92 simulation. The 300°C 5 min^{-1} RTA sample has a near identical profile as the as-implanted sample. After 350°C or 450°C annealing, the hydrogen peak concentration drops significantly, but the profiles are not broader. The hydrogen distributions are also measured using hydrogen forward scattering (HFS). The sampling area by HFS is on the order of a couple of millimeters and much larger than that of SIMS. The total observed hydrogen doses from both SIMS and HFS are depicted in Fig. 5. There is a discrepancy on the absolute value of the hydrogen dose due to systematic errors in the SIMS data. The dose value from SIMS data is generally less accurate (±20% error) due to its indirect calibration method and matrix effects in the presence of a high concentration of hydrogen. On the other hand, HFS experiments have less error in the absolute value, and the HFS measurement results agree well with the dose value calibrated by the hydrogen implantation current. Nevertheless, a similar dose variation trend is observed from both the techniques. The hydrogen profile and total dose are largely preserved after annealing up to 350°C, just before exfoliation takes place. According to the experimental results published in the literature [48], hydrogen diffuses very fast in silicon. The diffusion coefficients (D) and characteristic diffusion lengths $(Dt)^{1/2}$ during a 5 min annealing is given in Table 1. The diffusion lengths are at least nine times larger than the hydrogen projected range (0.42 μm). Apparently, the hydrogen will readily diffuse out of surface during annealing if there is no hydrogen nucleation mechanism underneath the silicon surface.

It is easy to comprehend a minimum hydrogen dose threshold below which silicon cleavage cannot occur. interestingly, there is also a maximum hydrogen dose threshold above which no silicon exfoliation will take place. For a sample implanted with 1.6×10^{17} cm^{-2} hydrogen (implantation charge readings), neither microcavity formation nor silicon layer cleavage can be observed at various annealing schemes between 200°C and 900°C. HFS experimental results reveal that the as-implanted sample dose is at 8.6×10^{16} cm^{-2} that is well below the implantation dose reading. One speculation is that some of the implanted hydrogen diffuses out even at room temperature at such a high hydrogen concentration. The retained dose after a 350°C anneal is 7.6×10^{16} cm^{-2} and 12% less than the as-implanted value. The retained dose for 450°C, 5 min RTA is 4.8×10^{16} cm^{-2}. The phase transformation in the damaged layer may have caused the upper dose threshold.

Table 1
Hydrogen diffusion coefficient and characteristic diffusion lengths

Temperature (°C)	Diffusion coefficient $D(10^{-10}$ cm^2 s$^{-1})$	Characteristic diffusion length $(Dt)^{1/2}$ (μm)
300	5.3	4.0
350	13	6.2
400	28	9.2
450	55	13
500	98	17

Evidently, the silicon layer damage is much more severe in the case of 1.6×10^{17} cm^{-2} hydrogen implantation. At such a high dose, the damage layer is either no longer favorable for hydrogen nucleation and microcavity growth, or its mechanical properties have changed dramatically preventing fracture growth. The phase transformation argument is supported by RBS channeling results. The sample with a retained dose of 1.6×10^{17} cm^{2} shows a peak dechanneling yield of 0.94, while the peak dechanneling yield for the 4.0×10^{16} cm^{-2} sample is only 0.48.

Based on the hydrogen dose measurement results, internal stress exerted by the buried hydrogen molecules can be estimated using the ideal gas law. Assuming a hydrogen implantation dose of 5×10^{16} cm^{-2} with half of the hydrogen being nucleated inside the microcavities after annealing and that the microcavities have a uniform thickness of 1 nm (determined by XTEM), the H_2 molecule density in the cavities is 1.3×10^{23} cm^{-3}. Using the ideal gas law, the internal pressure inside the microcavities at 300°C can be calculated. The pressure values are plotted in Fig. 6 as a function of the effective microcavity area ratio defined by the areas covered with microcavities normalized by the whole wafer cross-sectional area. They hydrogen gas pressures are in Giga-Pascal (GPa) range. Previously reported fracture stress values for single crystal silicon are in the range of 6.1 GPa using a microbeam setup experiment [49]. It is also expected that the fracture stress in the hydrogen peak regions could be less than the perfect silicon crystal value, considering the fact that hydrogen super-saturation and implantation damage can generate many dangling bonds in silicon. This simple calculation supports the argument that the internal pressure inside the microcavities is strong enough to break the Si–Si bond, thereby spurring surface layer cleavage.

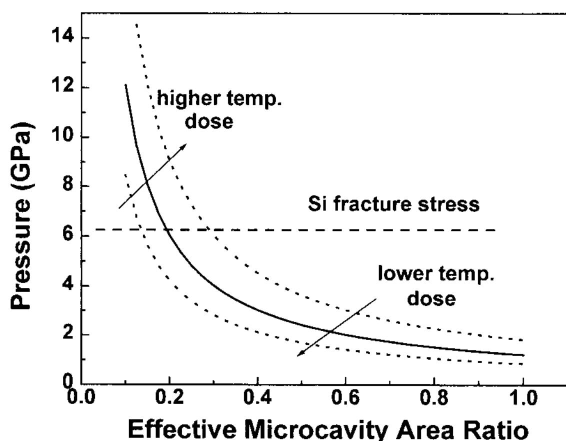

Fig. 6. Microcavity internal pressure vs. the effective area ratio. The retained hydrogen dose is taken to be 5×10^{16} cm^{-2}, and the annealing temperature is at 300°C. The calculated internal pressure is based on the ideal gas law. The pressure increases linearly with higher doses and higher annealing temperatures. Fig. 1: Thickness of the top silicon layer of the SOI wafer at various radial locations determined by Alpha-step measurements.

3. Light emitting buried porous silicon fabricated by hydrogen PIII

In the last few years, strong room-temperature light emission from electrochemically etched porous silicon (PS) [50,51] has attracted a lot of attention as the technology has the potential to integrate optoelectronic and microelectronic devices on a single Si wafer. Unfortunately, the chemically etched PS process is difficult and not compatible with traditional Si fabrication technology because the HF solution that is the anodic electrolyte [50] causes a rough surface and leaves surface impurities after the etching process [52]. Furthermore, the mechanism of light emission from PS is still unclear. An alternative way to prepare 'clean' PS is by the generation of nano-sized bubbles beneath the surface using hydrogen PIII. The method avoids contamination from acid and has higher compatibility with Si-based IC fabrication [53]. When the silicon walls between these bubbles are thin enough to allow quantum effects to take place, silicon will be transformed from an indirect band gap material to a direct band gap one and will give out light at an energy higher than the silicon band gap. The structure of the resulting buried porous silicon (BPS) is similar to that of ordinary porous silicon.

The 77 K photoluminescence (PL) spectrum exhibited in Fig. 7 is acquired at an excitation wavelength of 514.5 nm from a silicon wafer after 5 kV hydrogen PIII [54]. There are two broad fluorescent bands in the as implanted sample: 1010 and 890 nm (curve c in Fig. 7). By comparing to the PL spectrum of pure Si wafer obtained under the same conditions, the 890 nm peak represents an instrumental background. The small peak at 1100 nm in the pure Si PL spectrum corresponds to the band to band emission of Si. Its energy is equivalent to the Si indirect band gap. Hence, the band located at 1010 nm is believed to originate from the buried porous silicon. The full-width half-maximum (FWHM) of this band is about 0.2 eV. The BPS emission band can still be observed after annealing at 325°C for 1 h, but almost disappears after annealing at 670°C for 2 h. As suggested by D. Bisero et al. [55], this is due to the coarsening of the bubbles during the annealing process as well as the loss of hydrogen from the silicon wafer when the annealing temperature exceeds 400°C. The implanted hydrogen can passivate nonradiative recombination centers stemming from defects and dangling bonds and consequently increase the efficiency of light emission.

Fig. 8 shows the SIMS results of two samples implanted under similar conditions but differing in implantation time: #1 for 1 min and #2 (the same sample described above) for 10 s. In general, the implantation dose should increase linearly with implantation time. However, based on the SIMS results, the hydrogen doses in samples #1 and #2 are 3.2×10^{14} and 3.8×10^{16} cm^{-2}, respectively. This reverse trend can be attributed to the heat created during PIII. As there is no sample cooling, the wafer temperature goes up significantly during PIII as a large number of ions

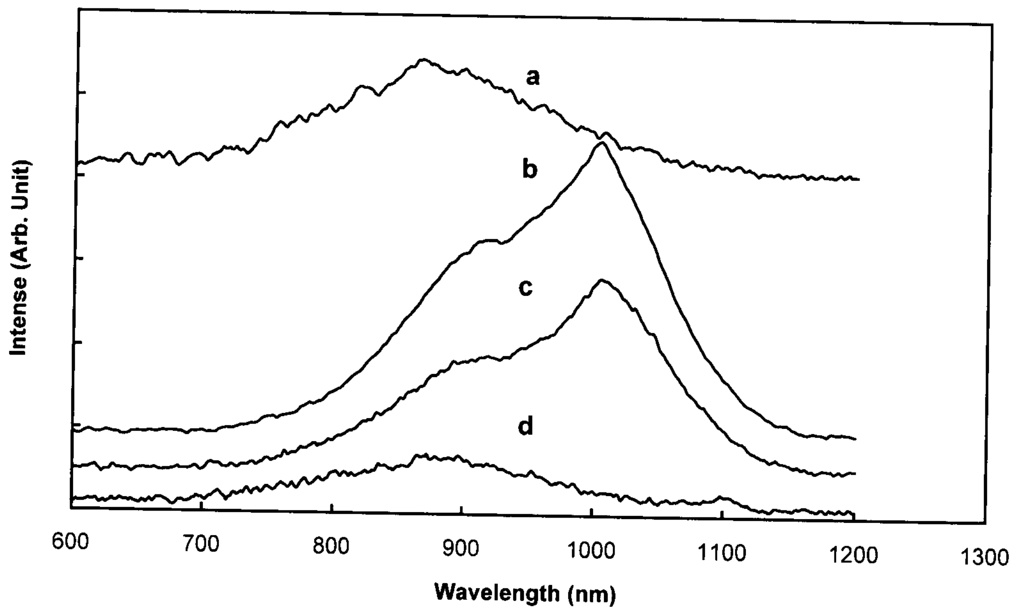

Fig. 7. Photoluminescence (PL) spectra of pure silicon (curve d) and hydrogen implanted samples: (a) 670°C, 2 h annealing, (b) 325°C, 1 h annealing, and (c) as implanted.

impact the wafer at the same time. By observing the color of the wafers during the implantation experiment, the substrate temperature is believed to exceed 500°C after 1 min. After the plasma source and the high voltage power supplier are turned off, the wafer is allowed to cool to room temperature in the vacuum chamber before it is taken out. This waiting process which can take up to an hour is similar to thermal annealing in vacuum. More hydrogen diffusion is thus expected for sample #1 because of the higher temperature, whereas the short implantation time and subsequently the lower substrate temperature for sample #2 result in a higher retained hydrogen dose in the sample. This phenomenon is supported by the PL data. Sample #2 shows strong luminescence at 77 K while that in sample #1 is undetectable. In addition, the hydrogen dose in sample #1 is not sufficient to passivate the nonradiative recombination centers. There-

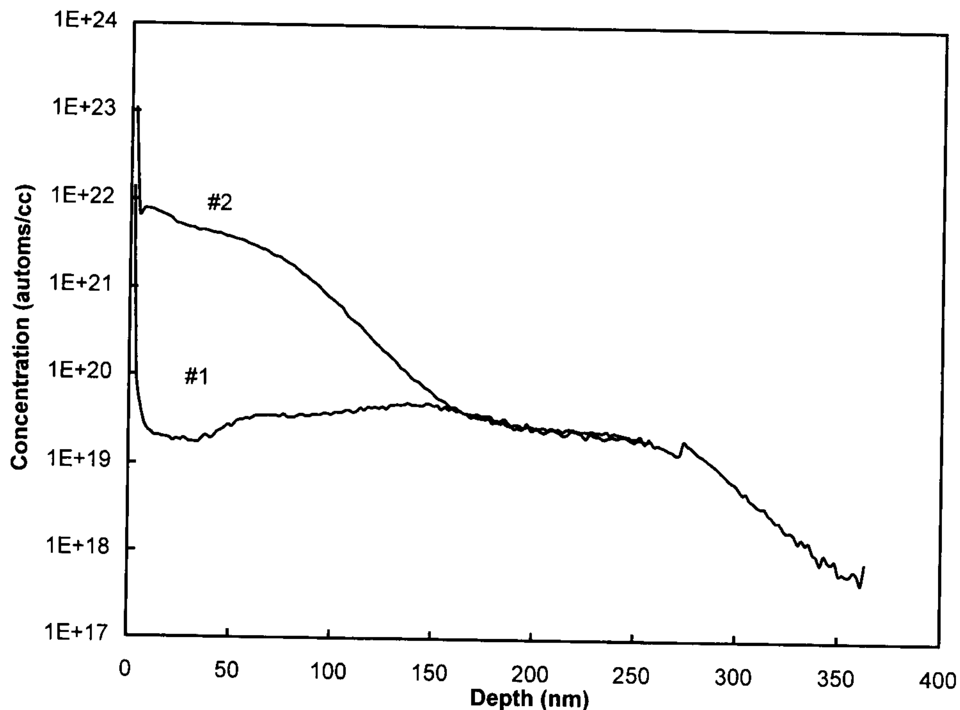

Fig. 8. SIMS hydrogen depth profiles of two samples implanted at −5 kV the gas pressure at 0.5 mT.

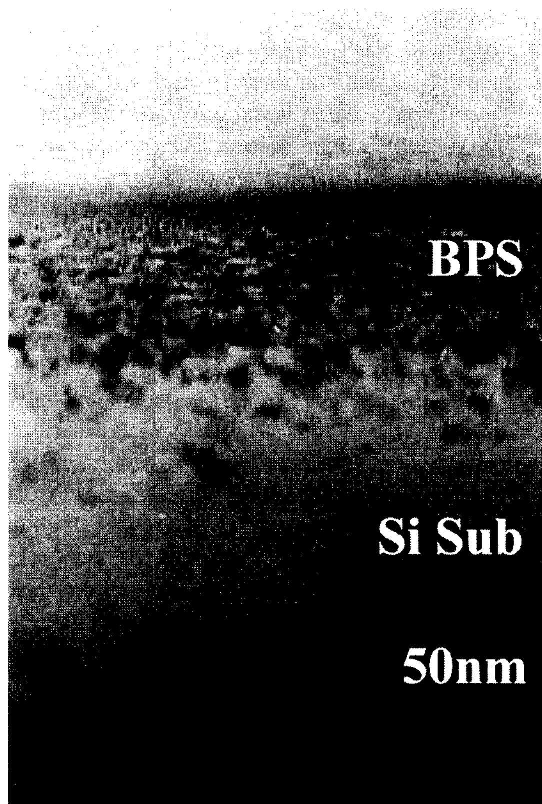

Fig. 9. XTEM picture of buried porous silicon (BPS).

fore, the possibility of excited carriers recombining through the radiative path is low. Pavesi et al. [56] have shown no luminescence from the as-implanted samples, and a salient fluorescence band can be observed only after annealing at 200°C or higher. The as-implanted samples show strong fluorescence at 77 K. This is believed to be caused by the unintentional 'annealing process' from the high ion flux during the PIII experiments as explained above.

The XTEM image in Fig. 9 reveals a large number of bubbles under the surface. The projected range of BPS is about 50 nm. The Si absorption coefficient of photons at an energy of 1.5 eV is 0.78×10^{3} cm^{-1} [57]. Therefore, the emitted light from the underlying BPS layer penetrates the thin overlay unattenuated. Even if the light energy shifts to 2.5 eV (blue), the transmission loss will still be minimal and 91% of the fluorescent light can be transmitted. This has important ramification, if indeed both photonic and microelectronic devices can be fabricated in the same substrate. The BPS materials are also believed to be more stable than the electrochemically etched counterparts for they are protected by the overlayer.

4. Impurity gettering using microcavities created by helium PIII

Interests in the properties of helium-induced cavities have spurred research activities in conventional helium implantation as well as plasma immersion ion implantation into silicon as the clean inner surface of cavities facilitates the study of surface phenomena. A number of studies on helium implantation have reported the formation of cavity microstructures and their thermal evolution [58–61]. The bubbles in the as-implanted Si are only a few nanometers in diameter. A post-implantation annealing step at a temperature higher than 700°C causes the helium to diffuse out of silicon, leaving behind the cavities. Hakvoort et al. [62] have reported that these cavities are stable up to at least 800°C. Bangert et al. [63] have suggested that oxygen can influence the formation of cavities. Evans et al. [64] have shown the inhibiting role of oxygen on the diffusion of bubbles or cavities. They have also confirmed that even a comparatively small dose of oxygen has a marked effect on the annealing behavior of the bubbles and cavity. They have also confirmed that even a comparatively small dose of oxygen has a marked effect on the annealing behavior of the bubbles and cavity evolution.

Gettering is a process by which metallic impurities are removed from the active regions of devices to favorable trapping or precipitation sites. The more traditional internal gettering process utilizes oxygen precipitates in the bulk of a Czochralski (CZ) silicon wafer to remove impurities from the near surface active region. Ion implantation is an effective method to introduce gettering centers [65,66]. The highly reactive silicon dangling bonds on the inner surface of helium bubble induced cavities can be terminated by hydrogen, oxygen or other elements, and these cavities can also act as gettering centers. Myer et al. [67] and Wong-Leung et al. [68,69] have demonstrated the effective gettering of Cu and Au by internal cavities in Si produced by helium and hydrogen implantation, respectively. Their results indicate that gettering remains stable for annealing up to 850°C. The use of PIII for implantation of helium and oxygen to form the gettering layer has the benefits of a high implantation dose rate, large area implantation and hence, a short implantation time independent of wafer size.

The gettering characteristics of microcavities created by He PIII have been investigated by plasma implanting silicon wafers with 2×10^{17} cm^{-2} He^{+} at 600°C [70]. The synergistic effects of oxygen have also been studied by plasma implanting a second set of samples with a combination of He^{+} and O_2^{+}. In this example, O_2^{+} ions are implanted at 65 kV for 1 min and 3 min to achieve implantation dose of 4×10^{16} (LD sample) and 1.7×10^{17} cm^{-2} (HD sample), respectively. After PIII, Cu or Au is deposited and diffused from both sides of the wafers. the diffusion is performed at 1200°C for 2 h in nitrogen followed by an additional 1 h annealing at 900°C. The gettering annealing sequence is the same as that of diffusion and the gettering stability can be assessed by repeating the annealing cycle on the samples.

The SIMS depth profiles of Cu and Au gettered by helium microcavities are shown in Fig. 10. The sample used to investigate the gettering of Cu is implanted with He^{+} at 20 kV which introduces a band of cavities located at a depth

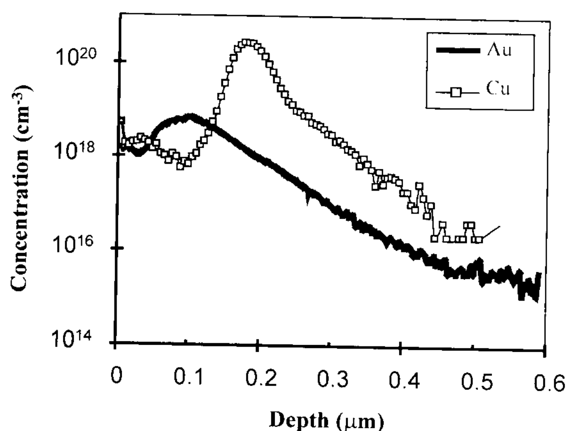

Fig. 10. SIMS depth profiles of Cu and Au showing gettering by helium cavities. Cu gettered sample corresponds to He^+ implantation at 8 kV. Cu gettered sample corresponds to He^+ implantation at 20 kV. The implantation dose in both cases is 2×10^{17} cm^{-3}. Au and Cu are diffused at 1200°C for 2 h. The SIMS analysis was performed using a 10 kV Cs^+ primary ion beam and a CAMECA IMS-4F. The depth scale was calibrated based on stylus profilometric measurement of the sputtered crater.

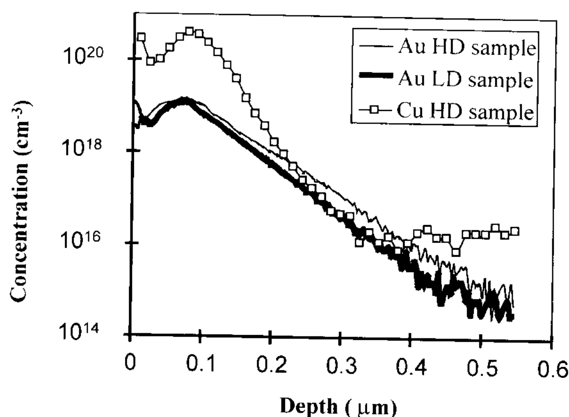

Fig. 11. SIMS depth profile of Au and Cu showing gettering by helium cavities and oxygen precipitates. The Au HD-sample corresponds to an implantation dose of 2×10^{17} cm^{-2} of He^+ at 8 kV followed by an implantation dose of 1.7×10^{17} of O_2^+ cm^{-2} at 65 kV. The Au LD-sample corresponds to an implantation dose of 2×10^{17} cm^{-2} of He^+ at 8 kV followed by an implantation dose of 4×10^{16} cm^{-2} of O_2^+ at 65 kV. The Cu HD-sample corresponds to an implantation dose of 2×10^{17} cm^{-2} of He^+ at 8 kV followed by an implantation dose of 1.7×10^{17} cm^{-2} of O_2^+ at 65 kV. The SIMS analysis was performed using a 10 kV Cs^+ primary ion beam and a CAMECA IMS-4F. The depth scale was calibrated based on stylus profilometric measurement of the sputtered crater.

of 210 nm with a straggle of 105 nm. The peak of the Cu profile in Fig. 10 is at a depth of approximately 200 nm with a width of about 240 nm corresponding to the expected band of helium-induced cavities. The gold gettered sample is implanted by He^+ at 8 kV. The SIMS depth profile of Au reveals a peak at a depth of 95 nm with a straggle of approximately 110 nm. These results indicate that the well-defined band of helium-induced cavities act as an effective gettering sink for both Cu and Au. A small peak near the surface in both the Cu and Au profile is seen and it is probably due to a SIMS surface artifact.

The XTEM micrograph of the as-implanted HD sample shows a well defined band of helium-induced cavities of 8 nm to 50 nm in diameter. The SIMS depth profiles of Au in the HD and LD samples are shown in Fig. 11. It indicates that Au is indeed trapped in the region containing both the helium-induced cavities and oxygen precipitates. The concentration of gettered Au is 1.41×10^{14} and 1.05×10^{14} cm^{-2} in the HD and the LD samples, respectively. Even though more Au is observed in the HD sample, the difference between the two samples is not proportional to the oxygen doses. It is quite clear, in spite of the fact that both oxygen precipitates and helium-induced cavities form individual gettering sites, the presence of both structures in the same region does not enhance the gettering efficiency linearly. In fact, it is possible that some of the oxygen atoms may adsorb onto the sidewall of the cavities to tie up the dangling bonds, thereby decreasing the gettering capability of these cavities. It is also interesting to note that the amount of Au gettered in both samples is not very high and lower than the solubility at 1200°C.

The RBS spectrum of the HD sample that is subsequently diffused and gettered with Cu is shown in Fig. 12. The spectrum shows that copper with an aerial density of 1.9×10^{16} cm^{-2} is trapped at the depth of 95 nm corresponding to the He^+ implantation range. The annealing step at 1200°C is repeated in this sample to examine the stability of the gettering. The SIMS profile of Cu after the second annealing process is shown in Fig. 11. Copper remains trapped in the band of helium-induced cavities combined with oxygen precipitates illustrating the stability of the gettering structure during the second high temperature annealing step at 1200°C.

The results indicate that the gettering efficiency of the helium-induced cavities is higher for a higher oxygen dose,

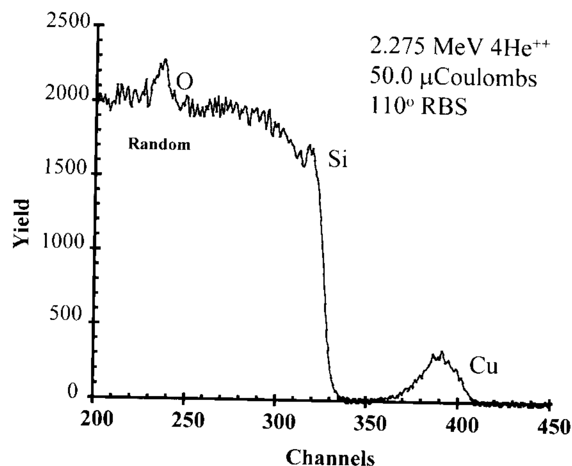

Fig. 12. RBS spectrum for the Cu HD-sample implanted with 2×10^{17} cm^{-2} of He^+ at 8 kV and subsequently implanted with 1.7×10^{17} cm^{-2} of O_2^+ at 65 kV. Cu is diffused and gettered by two annealing cycles up to 1200°C for 2 h.

even though this difference is not linear with the amount of oxygen introduced. The results also confirm that the gettering mechanism is stable during high temperature annealing at 1200°C. The PIII technique offers, independent of wafer area, an extremely high implantation dose rate and short implantation time when compared with conventional beam-line ion implantation. It is thus well suited for the incorporation of gettering sites into 200 nm and larger silicon wafers.

5. Ion-cut using PIII

As explained previously in this paper, the pressure exerted by the expanding microcavities formed by hydrogen or helium implantation is high enough to cause layer cleavage. An important application utilizing this exfoliation phenomenon is the fabrication of silicon-on-insulator (SOI) which offers many inherent benefits over bulk silicon substrates for deep sub-micrometer complimentary metal-oxide silicon (CMOS) device. Some of the advantages include lower parasitic capacitance, radiation hardness, higher packing density, latch-up immunity, less pronounced short-channel effects, and dielectric isolation [71,72]. The emerging technology is commercially referred to as Smart-Cut™ when employing conventional beam-line ion implantation [73,74]. We are using the terminology ion-cut here to reflect a broader scope that includes more than the fabrication of SOI and also incorporates the use of plasma immersion ion implantation. The ion-cut technology opens the window for many other exciting material synthesis opportunities for the electronic industry, such as silicon-on-glass [75], germanium, silicon carbide and diamond thin films [76], as well as three-dimensional devices [77,78].

5.1. Hydrogen PIII/ion-cut

As shown in Fig. 13, the ion-cut process starts with two bulk silicon wafers, with one or both wafers grown with thermal oxide [42]. Hydrogen is implanted into one of the silicon wafers with a thermal oxide layer (donor wafer). The implanted wafer is then bonded to the other silicon wafer (receptor wafer). During subsequent thermal treatment between 400°C and 600°C, the wafer pair breaks into two completely separated wafers along the hydrogen implanted region, and the receptor wafer has an SOI structure ($Si/SiO_2/Si$). The wafer surface is finally touch polished to make an integrated circuit grade SOI wafer [73,74]. In the ion-cut process, the required hydrogen dose is quite high (2×10^{16} to 1×10^{17} atoms cm^{-2}), and PIII is well suited for this high dose application. PIII may also provide some ion-cut process optimization opportunities, such as multiple ion implantation, surface plasma treatment for low temperature wafer bonding, and so on.

For the hydrogen PIII ion-cut process, simultaneous implantation of H^+, H_2^+, and H_3^+ may initiate cleavage at different depths. BY adjusting the hydrogen gas pressure, plasma power, and magnetic field, a hydrogen plasma with either H_2^+, or H_3^+ as the dominating ion species can be created. H_2^+ is the preferred species as it is dominant at the lower pressure regime that is required by the non-collisional conditions and it offers a larger implantation depth than H_3^+. In addition, the total ion density is also lower and sample heating can be minimized. By keeping the wafer temperature during PIII below 250°C, the implanted hydrogen is less likely to diffuse and nucleate during the implantation step. With proper tuning, the plasma condition can be achieved to yield over 90% H_2^+ ions, less than 10% H^+, and negligible H_3^+ ions. The secondary ion mass spectrometry (SIMS) profile of a 50 kV implanted sample is displayed in Fig. 14 showing that over 95% of the hydrogen dose is from $H_2{}^+$ while less than 5% originates from H^+. Very little $H_3{}^+$ ions are detected in the experiment. Two hydrogen peaks in the SIMS profile are in very good agreement with the TRIM92 simulation predicting a projected range of 0.296 µm for 50 kV H_2^+ and 0.493 µm for 50 kV H^+.

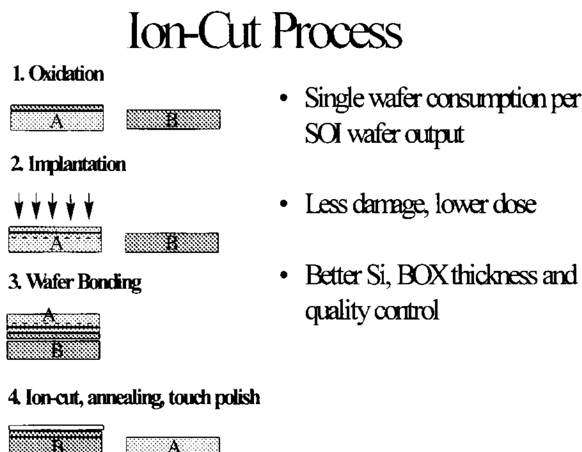

Fig. 13. Schematic of the PIII/ion-cut process.

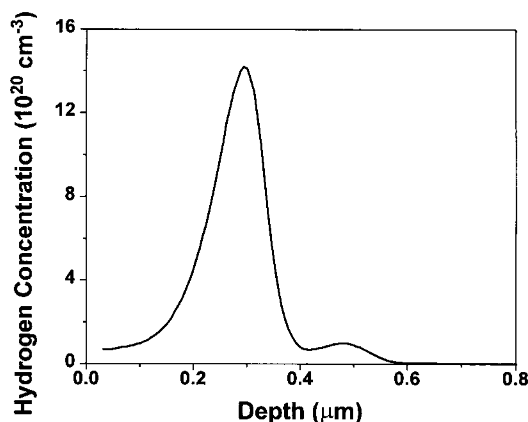

Fig. 14. SIMS profile of implanted hydrogen using PIII. The implantation energy is 50 kV. Over 95% of the hydrogen dose is from H_2^+ ions.

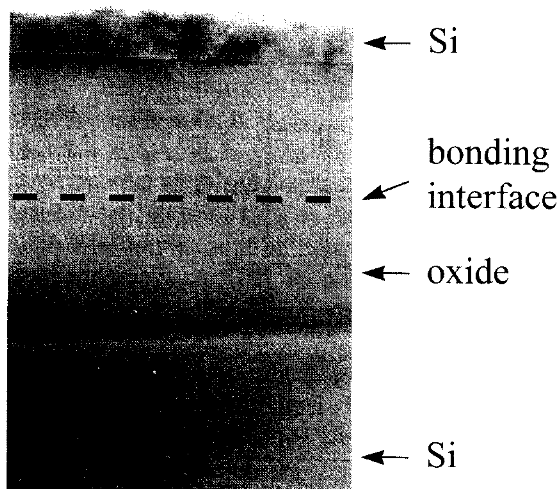

Fig. 15. XTEM micrograph of $Si/SiO_2/Si$ structure formed using hydrogen PIII/ion-cut. The top silicon wafer was implanted using hydrogen plasma at 35 kV with 10^{17} cm^{-2} nominal dose. The dashed line indicates the bonded oxide/oxide interface.

A $Si/SiO_2/Si$ structure formed using the hydrogen PIII ion-cut process is displayed in Fig. 15. The top silicon wafer was implanted using the H_2^+ dominated plasma at 35 kV and a nominal dose of 1×10^{17} cm^{-2}. The wafer separation is uniform across the sample surface, and there is no silicon layer separation along the H^+ or H_3^+ implanted region. The dashed line indicates the original bonded oxide/oxide interface. It is apparent that after 900°C, 60 min final annealing, there is no distinguishable interface in the bonded oxide layer.

5.2. Helium PIII/ion-cut

SOI structure can be also synthesized using helium PIII/ion-cut. The only ion species detected using the mass spectrometer is He^+, and there is no multiple ion species problem as confirmed by SIMS. The TRIM92 Monte Carol simulated helium projected range at 40 kV is 0.366 μm and about 20% higher than what we measured in the SIMS profile. The cross-section transmission electron microscopy (XTEM) image showing helium induced cleavage is exhibited in Fig. 16. The microcavities form along the (100) plane, very similar to that observed in hydrogen implanted samples. Fig. 17 shows the XTEM micrograph of a $SI/SiO_2/Si_3N_4/SiO_2/Si$ structure. In this case, a silicon wafer with a 20 nm oxide layer is implanted with helium at 33 kV with a nominal dose of 1×10^{17} cm^{-2}. It is bonded to another silicon wafer which has PECVD deposited oxide and nitride layers on the surface. The implanted wafer cracks along the implanted helium peak region during subsequent 500°C annealing. This SOI structure was finally annealed at 1100°C for 60 min to solidify the SiO_2/Si_3N_4 interface indicated by the dashed line in the image. In the helium PIII/ion-cut process, only small pieces of silicon a few microns in size, but very high in density, are successfully transferred to the other silicon wafer. It may be due to the more extensive crystal damage introduced by helium implantation. There are also 'bubble' shaped microcavities formed in the silicon layers. Further investigation is needed to understand and better optimize the helium induced silicon exfoliation and ion-cut process. However, this $Si/SiO_2/Si_3N_4/SiO_2/Si$ structure demonstrates that other than oxide and silicon, other materials such as Si_3N_4 can be incorporated in the SOI structure using the ion-cut process.

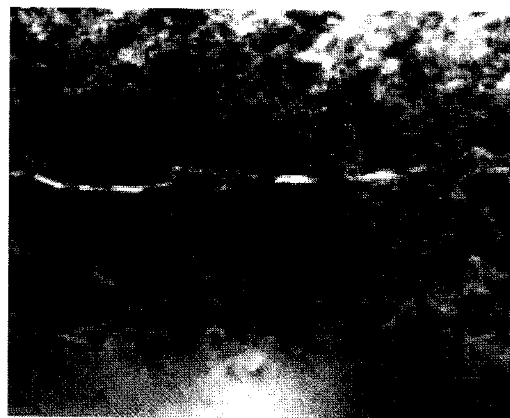

Fig. 16. XTEM image of helium induced microcavities inside silicon. Helium is implanted at 40 kV with a nominal dose of 10^{17} cm^{-2} using PIII. The sample was annealed at 600°C in a nitrogen ambient for 30 min.

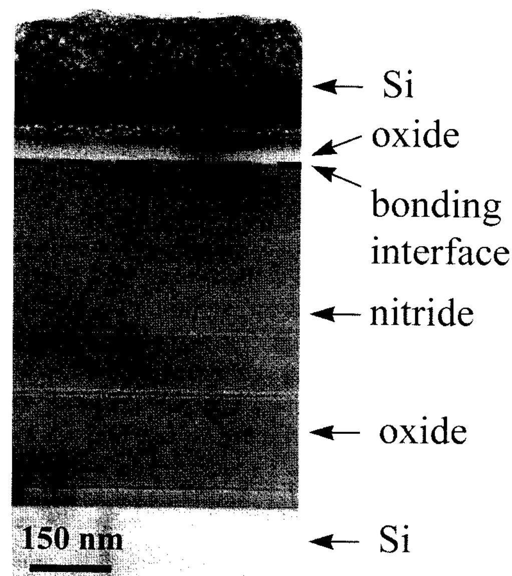

Fig. 17. XTEM micrograph of a $Si/SiO_2/Si_3N_4/SiO_2/Si$ structure formed using helium PIII/ion-cut process. The top silicon wafer was implanted using helium plasma at 33 kV with 10^{17} cm^{-2} nominal dose. The dashed line indicates the bonded oxide/nitride interface. There are extended crystal damage and microcavity formation in the silicon layers.

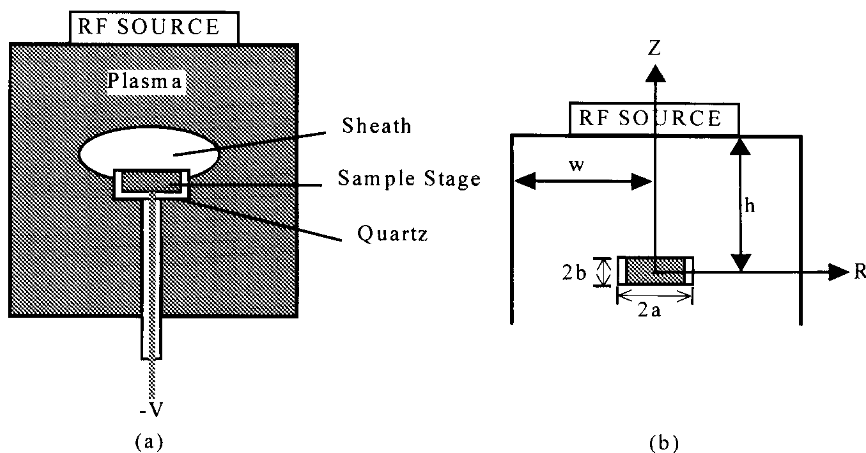

Fig. 18. (a) Schematic of the PIII equipment, (b) Model used in the simulation.

5.3. Implant nonuniformity induced by sample stage

Even though the feasibility of PIII as an ion-cut technique has been demonstrated, its commercial viability hinges on the quality of the resulting SOI wafers. One of the critical parameters is the thickness uniformity across the silicon wafer. Recently, it has been discovered that the implant uniformity is exacerbated by the insulating shroud used around the sample stage in conventional plasma immersion ion implanters. As PIII has traditionally been used in metallurgical and tribological applications, the equipment design is somewhat different from the ones used in the microelectronic industry. Since all surfaces exposed to the plasma and under a negative bias are implanted, including both the sample as well as the unprotected sample stage, it is not uncommon in PIII that a large portion of the implanted current is wasted on the sample stage. Quartz is usually used to cover the sample stage in order to reduce the wasted power, improve the implantation efficiency, and minimize metallic contamination arising from unintentional sputtering of the sample stage. However, the quartz cover strongly alters the electric field distribution around the sample and changes the ion trajectories. Consequently, ions are not implanted uniformly across the sample and it presents a big problem to semiconductor applications.

To investigate this effect, pure hydrogen is used to form the plasma and hydrogen is implanted into a silicon wafer 150 mm in diameter. The schematic of the PIII instrument is illustrated in Fig. 18(a) [43]. A patented radio frequency plasma source consisting of four coupling coils to improve plasma uniformity is positioned on top of the chamber. The stainless steel sample stage is placed in the center of the chamber. It consists of a cylindrical platen surrounded by a quartz shroud on the side and underneath. The platen is supported by a quartz-covered stainless steel rod and connected to an external power modulator. In the experiments, the sample is biased to -20 kV at 100 Hz. The pulse duration is 30 μs and the wafer is implanted at a hydrogen pressure of 0.4 mT for 30 min.

Fig. 19 depicts an optical photograph of the as-implanted Si wafer. The center (region A) of the wafer shows a grotesque feature referred to as an 'arcing spot'. The diameter of the arcing spot is around 1 cm. A white ring is observed at about 4 cm from the center (region C). The width of the white ring is about 3 mm. Under microscope, innumerable bubbles can be observed at the arcing spot and the white ring. It has been shown that a high dose of implanted hydrogen ($>4\times10^{15}$ ions cm^{-2}) can induce the formation of bubbles at temperature as low as 325°C [41,42,70]. The bubbles change the light reflection on the

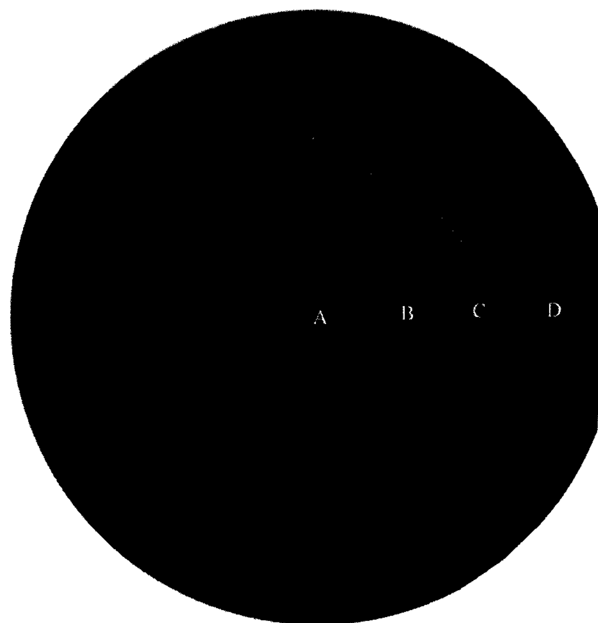

Fig. 19. Optical photograph of the as implanted 150 mm diameter Si wafer. The four distinct areas are marked.

silicon surface and can be detected with the naked eye. The visual appearance indicates that regions A (arcing spot) and C (white ring) have received a larger hydrogen dose. Though the wafer is not heated intentionally during implantation, the high ion flux causes some sample heating and it is believed that regions A and C reach a temperature as high as several hundred degrees Celsius during PIII.

To investigate the cause of the arcing spot and the white ring, a two-dimensional PIC (particle-in-cell) method [79] is used to simulate the implantation process [80]. The model is illustrated schematically in Fig. 18(b). The r-z origin (cylindrical coordinates) is the center of the sample holder. The initial velocities of the ions and electrons are chosen from a Maxwellian distribution having 0.026 eV ions and 3.0 eV electrons. The simulation commences at time $t=0$ as soon as a negative voltage is applied to the sample stage. The time step is selected to be 10^{-10} s. To simplify the calculation, the following assumptions are made in our simulation code:

1. The processing chamber has a vertical symmetry, and only particles in the upper part are simulated. Ions and electrons have the same possibility moving from the upper part to the bottom part and vice versa. If an ion (or electron) moves from the upper part to the bottom part with velocity (V_r, V_z) and stops at position (r, z), another ion (or electron) must come from the bottom part to the upper part with velocity $(V_r, -V_z)$ and stop at position (r, z).
2. At a pressure of 0.4 mT, collisionless conditions are achieved.
3. Secondary electrons are not considered in our calculation as they do not contribute to the ion implantation dose.
4. Abrupt −20 kV pulses with zero rise-time are applied to the sample stage.
5. Ions around the quartz cover are accelerated by the electrical field and impinged onto the surface of the quartz cover as soon as a negative voltage is applied to the sample stage. It is assumed that quartz is an ideal insulator where the charge does not leak out but can be neutralized by incoming ions or electrons. Time to reach equilibrium is small and the equilibrium voltage on the quartz due to charging is negligible when compared with the high sample bias. The boundary condition on this side can thus be written as

$$\phi|_{r=a,0\leq z\leq b}=0 \tag{1}$$

6. The silicon wafer is considered to be a good conductor, and no charge is accumulated on the wafer surface. It has therefore, the same potential as the sample stage. The boundary condition then is:

$$\phi_{0\leq r\leq a,z=b}=V \tag{2}$$

where V is the voltage applied to the sample holder.

7. The plasma density is uniform throughout the process chamber and only H^+ ions are considered.

The potential ϕ is solved from the following Poisson's equation using a five-point finite-difference approach:

$$\frac{1}{r}\frac{\partial}{\partial r}\left(r\frac{\partial}{\partial r}\phi\right)+\frac{\partial^2}{\partial z^2}\phi=-\frac{\rho}{\varepsilon_0} \tag{3}$$

where ρ and ε_0 are the charge density and the permittivity of free space, respectively. The additional boundary conditions are:

$$\phi|_{r=w}=0 \tag{4}$$

$$\phi|_{z=h}=0 \tag{5}$$

As the time step is smaller than the inverse of the electron plasma frequency ω_{pe}, electron oscillation is observed at the beginning of the simulation. From the field distribution map, a strong electric field is created at the edge of the sample stage. This field directs ions to the center of the sample stage. Fig. 20 shows the calculated accumulated dose across the Si wafer. Salient peaks can be observed at the center and 39 mm on both sides from the center of the wafer. Comparing Figs. 19 and 20, our simulation results accurately model the white ring.

The model also predicts that the wafer center will receive the highest hydrogen dose while there are much fewer ions implanted into the edge region. The extra hydrogen ions implanted into the center will result in local heating and accelerate bubble formation. The arcing spot (region A) exhibited in Fig. 19 indeed confirms the prediction. The area between regions A and C is predicted to have a lower dose. The size of region B where uniform implantation can be achieved depends on the size and location of the quartz cover, applied voltage, and plasma density.

The hydrogen in-depth distributions and doses in the four regions are determined by secondary ion mass spectrometry (SMS). The SIMS hydrogen doses are shown in Fig. 21. The trend is similar to the model prediction, even though the relative difference is smaller. There are two reasons affecting the doses measured in region A (arcing spot) and region

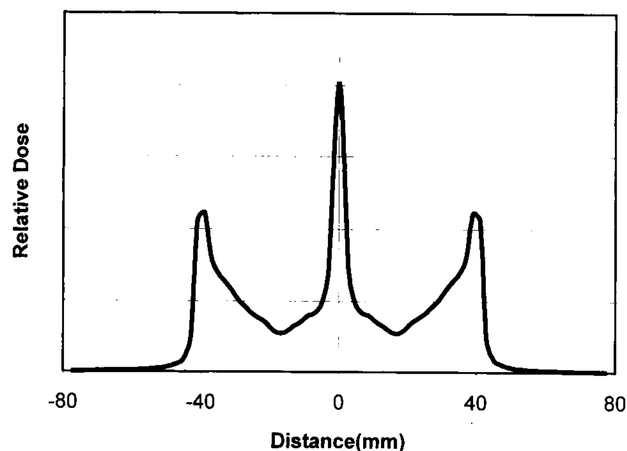

Fig. 20. Relative accumulated doses in the silicon wafer derived by our model.

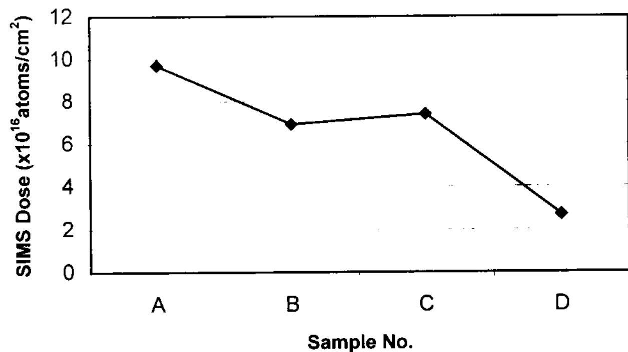

Fig. 21. Hydrogen doses determined in the four areas shown in Fig. 19 by SIMS.

C (white ring). Firstly, the surface roughness (due to bubbles) and matrix effects arising from the presence of microcavities make accurate SIMS quantification very difficult [70]. Secondly, hydrogen loss and diffusion during implantation can be substantial in the arcing spot and white ring since the areas are heated by the higher ion fluxes during PIII. The local temperature of the arcing spot and the white ring must be higher than 300°C since bubble formation can be observed [41]. The hydrogen diffusion coefficient at 300°C is 5.3×10^{-10} cm^2 s^{-1} [48], and the characteristic diffusion distance for 30 min is 9.7 µm. The projected range of hydrogen in Si is 250 nm by TRIM simulation and is much smaller than the characteristic diffusion distance. Hence, a substantial loss of hydrogen is expected from regions A and C during implantation. The SIMS results show a hydrogen dose of 2.7×10^{16} atoms cm^{-2} in region D (edge), but the model predicts much fewer implanted ions. It can be attributed to one of the assumptions. According to assumption #5, the potential abruptly changes from −20 kV at the edge of the sample stage to 0 kV on the quartz shroud. As a result, a very strong electrical field is created to expel ions from region D. However, in reality, this field is weaker than that assumed in our formalism.

The experimental and theoretical results suggest that the quartz shroud commonly used in PIII to reduce contamination and current demand on the modulator power supply alters the electric field and ion trajectories, and ions are selectively implanted into the center and a ring about 4 cm from the center. The theoretical model predicts that the location and dimension of the white ring will change with the applied voltage and plasma density. Hence, in order to reduce the focusing effects and improve the implant uniformity while limiting the total impacting ion current, the size and location of the quartz cover must be optimized.

5.4. Implant uniformity modeling

Using an optimized sample stage design, better uniformity can be achieved, but the results are still not perfect [81]. The residual thickness variation across a PIII/ion-cut wafer hampers the commercialization of the PIII/ion-cut

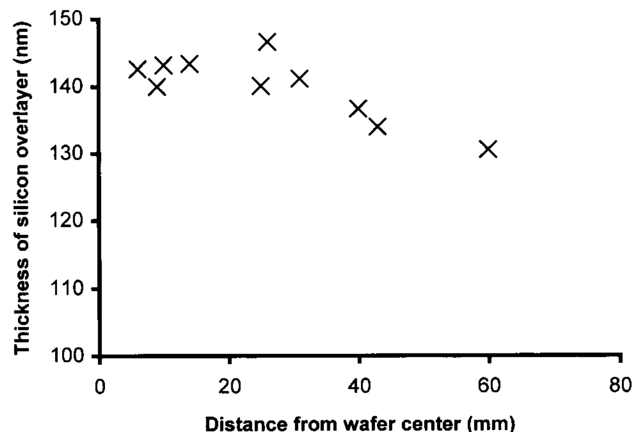

Fig. 22. Thickness of the top silicon layer of the SOI wafer at various radial locations determined by stylus profilometry.

technique. For an ion-cut process utilizing conventional beam-line ion implantation with mechanical scanning, the implantation energy and angle are same over the entire wafer. Any variation in the silicon film thickness thus depends on the cracking mechanism, that is, how smoothly the silicon layer separates along the microcavity plane. However, for PIII, since the whole wafer is implanted simultaneously inside the plasma, there is the possibility that the projected range of the implanted hydrogen can vary

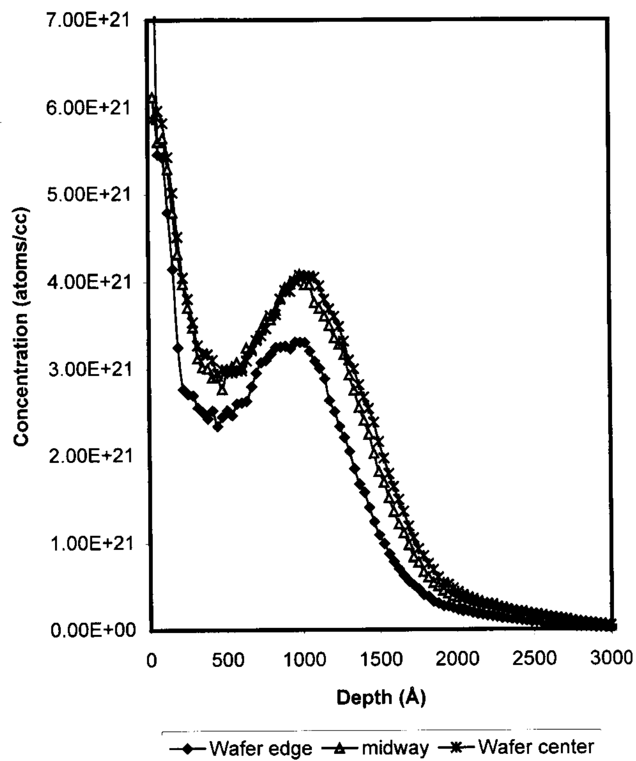

Fig. 23. Hydrogen depth profiles of the three regions on 150 mm wafer determined by SIMS: wafer center, 30 mm from center (midway), and 60 mm from center (wafer edge).

laterally on the wafer due to plasma non-uniformity and sample stage effects as described above. This is also true for beam-line ion implantation if electrostatic beam scanning is employed. A systematic study has been conducted to assess the thickness variation on a 150 mm SOI wafer produced by PIII and ion cut. Fig. 22 displays the thickness distribution of the silicon layer across the wafer as measured using Alpha-step stylus profilometry when no insulating shroud is used. The *x*-scale shows the distance of the measured area from the center of the wafer. It can be observed that the silicon overlayer thickness is quite uniform within a radius of about 35 mm and drops off toward the edge. The average thickness is 140 nm and the standard deviation is 5 nm. The thinnest silicon layer at 60 mm from the center is 90% of that in the center.

To investigate the origin of the thickness variation, SIMS analysis is conducted from samples taken from the center, 30 mm from the center, and 60 mm from the center and the hydrogen profiles are depicted in Fig. 23. A high concentration of surface hydrogen is observed just beneath the surface in all three samples but has been shown to be

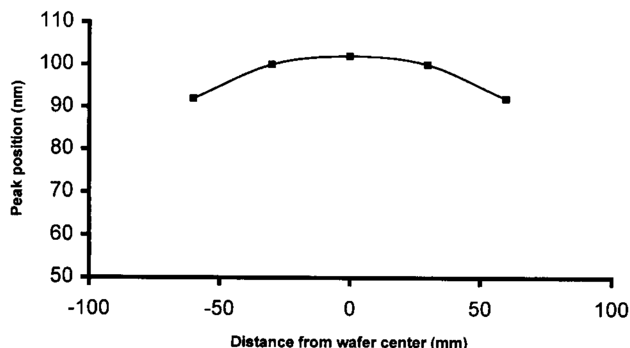

Fig. 24. Hydrogen projected range across the 150 mm silicon wafer determined by SIMS.

unimportant to the layer transfer process. Provided that the hydrogen dose is above a certain threshold value, the most important cracking parameter is the depth of the hydrogen peak at about 100 nm. Fig. 24 shows that the peak position is about the same in sample 1 (center) and sample 2 (30 mm from center) but shallower in sample 3 (60 mm from center).

Fig. 25. Potential distribution map for −20 kV implantation.

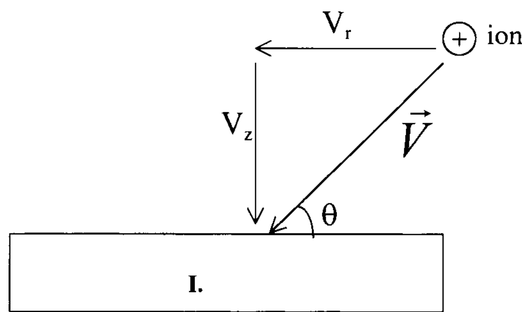

Fig. 26. Schematic diagram of the incident angle model.

The difference in the projected range between samples 1 and 3 is 9% and agrees well with the thickness data. It should be mentioned that the peak depth determined by SIMS and the thickness obtained by Alpha-step measurement differ by about 40 nm. The discrepancy is due to a SIMS artifact. In the presence of a large amount of hydrogen near the surface and peak, the sputtering rate is faster, and since an average sputtering rate is used in the depth calibration, the SIMS peak depths are shallower than they should be. However, the relative difference in the peak position is still valid as all three samples have similar hydrogen doses.

In PIII, it is usually assumed that ions impact the wafer at a normal angle. However, it is not the case in the vicinity of a corner such as the edge region of a silicon wafer. Fig. 25 displays the particle-in-cell (PIC) [79,82] simulation of the field lines around the silicon wafer on a sample stage of approximately the same size. It can be seen that the field lines are curved toward the wafer edge and ions will not impact the wafer at a normal angle. As shown in Fig. 26, there are two velocity components, V_r which is the radial velocity and V_z which is the axial velocity. The implantation angle θ is defined by

$$\tan(\theta) = \frac{V_z}{V_r} \tag{6}$$

The axial velocity determines how deep the ion will traverse into the silicon. Based on the field lines, ions implanted into the center of the wafer have a zero V_r, but the incident angle becomes progressively more glancing toward the edge. Fig. 27 depicts the incident angle (θ) and normalized projected range ($\sin\theta$) as a function of distance from the center. The results show that the impact angle and projected range are more or less constant within 40 mm from the center. Ions are implanted at a normal angle in this region. Closer to the edge, ions are collected not only from the region directly above but also from the side. The radial velocity component is increased and the incident angle is shallower resulting in a smaller projected range. The model predicts that the difference between the center and edge is about 10% and it correlates well with our experimental data. It implies that the observed thickness variation on the silicon wafer can be explained adequately by an oblique incidence model.

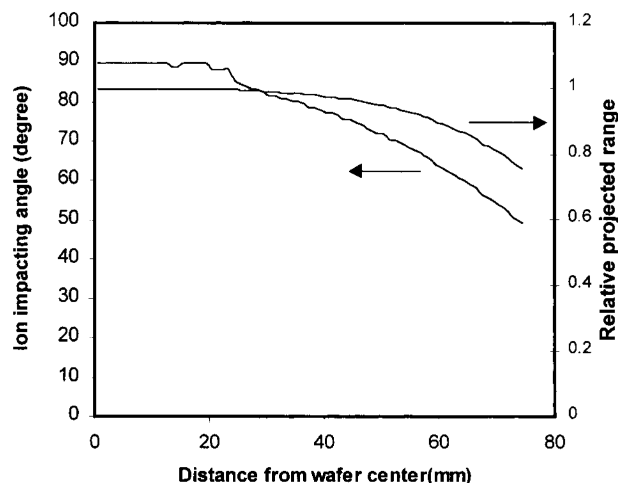

Fig. 27. Simulated incident angel (θ) and normalized project range ($\sin\theta$) across a 150 mm silicon wafer.

6. Conclusions

The microcavities formed by hydrogen or helium plasma immersion ion implantation have interesting characteristics. Their optical characteristic may one day enable the integration of photonic devices into integrated circuits. Impurity gettering has been demonstrated and PIII is thus a good method for the economic introduction of extra gettering sites into large wafers. Last but not the least, the PIII/ion-cut technique has been shown to be a viable method to fabricate silicon-on-insulator materials. Some of the factors affecting implant uniformity have also been reviewed. Using the proper instrumental design and experimental procedures, PIII emulates conventional beam-line ion implantation in the ion-cut or layer transfer process for silicon and other materials.

Acknowledgements

We would like to acknowledge the contribution of researchers at the City University of Hong Kong and University of California at Berkeley.

References

[1] J.R. Conrad, J.L. Radtke, R.A. Dodd, F.J. Worzala, N.C. Tran, J. Appl. Phys. 62 (1987) 4591.
[2] P.K. Chu, S. Qin, C. Chan, N.W. Cheung, L.A. Larson, Mat. Sci. Eng. Reports, R/17(6/7), 1996, p. 207.
[3] J.V. Mantese, I.G. Brown, N.W. Cheung, G.A. Collins, MRS Bulletin 21(8) (1996) 52.
[4] P.K. Chu, N.W. Cheung, C. Chan, Semiconductor Int. 6 (1996) 165.
[5] N.W. Cheung, Mat. Chem. Phys. 46 (1996) 132.
[6] N.W. Cheung, Nucl. Instr. and Meth. Phys. Res. B55 (1991) 811.
[7] X.Y. Qian, N.W. Cheung, M.A. Lieberman, S.B. Felch, R. Brennan, M.I. Current, Appl. Phys. Lett. 53 (1991) 348.

[8] C.A. Pico, X.Y. Qian, E. Jones, M.A. Lieberman, N.W. Cheung, Mat. Res. Soc. Proc. 223 (1991) 115.
[9] X.Y. Qian, N.W. Cheung, M.A. Lieberman, M.I. Current, P.K. Chu, W.L. Harrington, C.W. Magee, E.M. Botnik, Nucl. Instr. and Meth. Phys. Res. B55 (1991) 821.
[10] C.A. Pico, M.A. Lieberman, N.W. Cheung, J. Electronic Materials 21(1) (1992) 75.
[11] E.C. Jones, N.W. Cheung, IEEE Electron. Device Lett. 14(9) (1993) 444.
[12] D.L. Chapek, J.R. Conrad, R.J. Matyi, S.B. Felch, J. Vac. Sci. Technol. B12(2) (1994) 951.
[13] E.C. Jones, W. En, S. Ogawa, D.B. Fraser, N.W. Cheung, J. Vac. Sci. Technol. B12(2) (1994) 956.
[14] S. Qin, C. Chan, J. Vac. Sci. Technol. B12(2) (1994) 962.
[15] C. Yu, N.W. Cheung, Nucl. Instr. and Meth. Phys. Res. B79 (1993) 655.
[16] C. Yu, N.W. Cheung, IEEE Electronic Device Lett. 15(6) (1994) 196.
[17] T. Sheng, S.B. Felch, C.B. Cooper, J. Vac. Sci. Technol. B12(2) (1994) 969.
[18] S.B. Felch, R. Brennan, S.F. Corcoran, G. Webster, Nucl. Instr. and Meth. B74 (156) 1993.
[19] B. Mizuno, H. Nakaoka, M. Takase, A. Hori, I. Nakayama, M. Ogura, Proc. Int. Conf. on Solid State Devices and Materials, Osaka, Japan, 1995, p. 1041.
[20] R.J. Matyi, D.L. Chapek, D.P. Brunco, S.B. Felch, B.S. Lee, Surf. Coatings Technol. 93(2-3) (1997) 247.
[21] J. Shao, E.C. Jones, N.W. Cheung, Surf. Coatings Technol. 93(2-3) (1997) 254.
[22] M. Takase, B. Mizuno, IEEE Int. Sym. Semiconductor Manufacturing, San Francisco, 1997, B-9.
[23] S.B. Felch, D. Lenoble, M.J. Goeckner, Z. Fang, J. Galvier, A. Grouillet, 4th Int. Workshop on Plasma-Based Ion Implantation, Detroit, 1998, 2B-1.
[24] J.D. Bernstein, Qin Shu, C. Chan, T.J. King, IEEE Electronic Device Lett. 16(10) (1995) 421.
[25] C. Yu, N.W. Cheung, IEEE Electronic Device Lett. 15 (1994) 196.
[26] C. Yu, Z.L. Huang, N.W. Cheung, Proc. 11th IITC, 1992, p. 369.
[27] X.Y. Qian, M.A. Lieberman, N.W. Cheung, R. Brennan, M.I. Current, N. Jha, Nucl. Instr. and Meth. B55 (1991) 898.
[28] X.Y. Qian, M.H. Kiang, J. Huang, D. Carl, M.A. Lieberman, N.W. Cheung, I.G. Brown, K.M. Yu, M.I. Current, Nucl. Instr. and Meth. B55 (1991) 888.
[29] X.Y. Qian, M.H. Kiang, N.W. Cheung, I. Brown, X. Godechot, J.E. Galvin, R.A. MacGill, K.M. Yu, Nucl. Instr. and Meth. B55 (1991) 893.
[30] M.H. Kiang, C.A. Pico, M.A. Lieberman, N.W. Cheung, X.Y. Qian, K.M. Yu, Proc. Mat. Res. Soc. 223 (1991) 377.
[31] M.H. Kiang, C.A. Pico, J. Tao, R.A. Stewart, N.W. Cheung, M.A. Lieberman, Proc. Mat. Res. Soc. 223 (1991) 377.
[32] M.H. Kiang, J. Tao, W. Namgoong, C. Hu, M. Liberman, N.W. Cheung, H.K. Kang, S.S. Wong, Proc. Mat. Res. Soc. 265 (1992) 187.
[33] M.H. Kiang, M.A. Liberman, N.W. Cheung, X.Y. Qian, Appl. Phys. lett. 60 (1992) 2767.
[34] Z. Zhou, S. Qin, C. Chan, P.K. Chu, MRS Spring Meeting, San Franciso, 13–17 April, 1998.
[35] J.B. Liu, S.S. Iyer, R. Gronsky, C. Hu, N.W. Cheung, J. Min, P.K. Chu, Appl. Phys. Lett. 67 (1995) 2361.
[36] J. Min, P.K. Chu, Y.C. Cheng, J.B. Liu, S. Im, S. Iyer, N.W. Cheung, Solid State Technol. 40(5) (1997) S9.
[37] J. Min, P.K. Chu, Y.C. Cheung, J. Liu, S.S. Iyer, N.W. Cheung, Surf. Coating Technol. 82(1-2) (1996) 60.
[38] P.K. Chu, X. Lu, S.S.K. Iyer, N.W. Cheung, Solid State Technol. 40(5) (1997) S9.
[39] X. Lu, S.S.K. Iyer, J.B. Liu, C.M. Hu, N.W. Cheung, J. Min, P.K. Chu, Appl. Phys. Lett. 70(13) (1997) 1748.
[40] S.S.K. Iyer, X. Lu, J.B. Liu, J. Min, Z. Fan, P. Chu, C.M. Hu, N.W. Cheung, IEEE Trans. Plasma Sci. 25(5) (1997) 1128.
[41] X. Lu, N.W. Cheung, M.D. Strathman, P.K. Chu, B. Doyle, Appl. Phys. Lett. 71(13) (1997) 1804.
[42] X. Lu, S.S.K. Iyer, C.M. Hu, N.W. Cheung, J. Min, Z.N. Fan, P.K. Chu, Appl. Phys. Lett. 71(19) (1997) 2767.
[43] P.K. Chu, S. Qin, C. Chan, N.W. Cheung, P.K. Ko, IEEE Trans. Plasma Sci. 26(1) (1998) 79.
[44] M.K. Weldon, V. Marsico, Y.J. Chabal, S.B. Christman, E.E. Chaban, D.C. Jacobson, J.B. Sapjeta, A. Pinczuk, B.S. Dennis, A.P. Mills, C.A. Goodwin, C.M. Hsieh, Proc. IEEE Int. SOI Conf., Sanibel Island, FL, 1996, p. 150.
[45] M.K. Weldon, V. Marsico, Y.J. Chabal, A. Agarwal, D.J. Eaglesham, J.B. Sapjeta, W.L. Brown, D.C. Jacobson, Y. Caudano, S.B. Christman, E.E. Chaban, J. Vac Sci. Technol. B 15(4) (1997) 1065.
[46] Q.Y. Tong, T.H. Lee, K. Gutjahr, S. Hopfe, U. Gosele, Appl. Phys. Lett. 70 (1997) 1390.
[47] T. Poumeyrol, Study of the mechanism of transfer in the smart-cut process: application to the making of SOI material, Ph.D. Thesis, France, 1996.
[48] O. Madelung, Data in Science and Technology: Semiconductors, Springer, New York, 1991.
[49] F. Ericson, J.A. Schweitz, J. Appl. Phys. 68 (1990) 5840.
[50] L.T. Canham, Appl. Phys. Lett. 57 (1990) 1046.
[51] W. Skorupa, XIIth Int. Conf. Ion Implantation Technol., Kyoto, Japan, 1998, Th-2.
[52] L.T. Canham, M.R. Houlton, W.Y. Leong, C. Pickering, M.J. Keen, J. Appl. Phys. 70 (1992) 422.
[53] R. Siegele, G.C. Weatherly, H.K. Haugen, D.J. Lockwood, Appl. Phys. Lett. 66 (1995) 1319.
[54] Z. Fan, P.K. Chu, X. Lu, S.S.K. Iyer, N.W. Cheung, MRS Sym. Proc. 452 (1997) 427.
[55] D. Bisero, F. Corni, C. Nobili, R. Tonini, G. Ottaviani, C. Mazzoleni, L. Pavesi, Appl. Phys. Lett. 67 (1995) 3447.
[56] L. Pavesi, G. Giebel, R. Tonni, F. Corni, C. Nobili, G. Ottaviani, Appl. Phys. Lett. 65 (1994) 454.
[57] O. Madelung, Semiconductors Group IV Elements and III–V Compounds, Springer, Berlin, 1991, p. 20.
[58] C.C. Griffioen, J.H. Evans, P.C. De Jong, A. van Veen, Nucl. Instr. and Meth. B27 (1987) 417.
[59] D.M. Follstaedt, D.M. Myers, H.J. Stein, MRS Symp. Proc. 279 (1994) 105.
[60] C.H. Seager, S.M. Myers, R.A. Anderson, W.L. Warren, D.M. Follstaedt, Phys. Rev. B 50 (1994) 2458.
[61] R. Siegele, G.C. Weatherly, H.K. Haugen, D.J. Lockwood, L.M. Howe, Appl. Phys. Lett. 66 (1995) 1319.
[62] R.A. Hakvoort, A. van Veen, P.E. Mijnarends, H. Schut, Appl. Surface Sci. 85 (1995) 271.
[63] U. Bangert, P.J. Goodhew, C. Jeynes, I.H. Wilson, J. Phys. D19 (1986) 589.
[64] J.H. Evans, A. van Veen, C.C. Griffioen, Nucl. Istr. and Meth. B28 (1987) 360.
[65] T.M. Buck, K.A. Pickar, J.M. Poate, Appl. Phys. Lett. 21 (1972) 485.
[66] H. Wong, N. Cheung, P.K. Chu, Appl. Phys. Lett. 52 (1988) 889.
[67] S.M. Myer, D.M. Follstaent, D.M. Bishop, MRS Symp. Proc. 316 (1994) 33.
[68] J. Wong-Leung, C.E. Ascheron, M. Petravic, R.G. Elliman, J.S. Williams, Appl. Phys. Lett. 66 (1995) 1231.
[69] J. Wong-Leung, E. Nygren, J.S. Wlliams, Appl. Phys. Lett. 67 (1995) 416.
[70] J. Min, P.K. Chu, X. Lu, S.S.K. Iyer, N.W. Cheung, Thin Solid Films 300 (1997) 64.
[71] J.P. Colinge, Silicon-on-Insulator Technology: Materials to VLSI, Kluwer Academic Publishers, Boston, 1991.
[72] S. Cristoloveanu, S.S. Li, Electrical Characterization of Silicon-on-Insulator Materials and Devices, Kluwer Academic Publishers, Boston, 1995.

[73] M. Bruel, B. Aspar, B. Charlet, C. Maleville, T. Poumeyrol, A. Soubie, A.J. Auberton-Herve, J.M. Lamure, T. Barge, F. Metral, S. Trucchi, Proc. IEEE Int. SOI Conf., Tucson, Arizona, 1995, p. 178.
[74] M. Bruel, Nucl. Instr. and Meth. Phys. Res. B 108 (1996) 313.
[75] Q.Y. Tong, T.H. Lee, W.J. Kim, T.Y. Tan, U. Gosele, H.M. You, W. Yun, J.K.O. Sin, 1996 IEEE Intl. SOI Conf. Proc., Sanibel Island, FL, 1996, p. 36.
[76] Q.Y. Tong, T.H. Lee, K. Gtjahr, S. Hopfe, U. Gosele, Appl. Phys. Lett. 70 (1997) 1390.
[77] B.H. Lee, G.J. Bae, K.W. Lee, G. Cha, W.D. Kim, S.I. Lee, T. Barge, A.J. Auberton-Herve, J.M. Lamure, Proc. IEEE Int. SOI Conf., Sanibel Island, FL, 1996, p. 114.
[78] B. Aspar, M. Bruel, M. Zussy, A.M. Cartier, Electronics Lett. 32 (1996) 1985.
[79] C.K. Birdsall, A.B. Langdon, Plasma Physics via Computer Simulation, McGraw-Hill, New York, 1985.
[80] Z. Fan, P.K. Chu, C. Chan, N.W. Cheung, Appl. Phys. Lett. 73(2) (1998) 202.
[81] Z. Fan, P.K. Chu, N.W. Cheung, C. Chan, IEEE Trans. Plasma Sci., submitted.
[82] D. Wang, T. Ma, X. Deng, J. Vac. Sci. Technol. B 12 (1994) 905.